



1 **Determining the Daytime Earth Radiative Flux from National**
2 **Institute of Standards and Technology Advanced Radiometer**
3 **(NISTAR) Measurements**

4 WENYING SU¹, PATRICK MINNIS², LUSHENG LIANG², DAVID P. DUDA²,
Konstantin Khlopenkov², Mandana M. Thieman², Yinan Yu³, Allan Smith³,
Steven Lorentz³, Daniel Feldman⁴, Francisco P. J. Valero⁵

¹*Science Directorate, NASA Langley Research Center, Hampton, Virginia*

²*Science Systems & Applications, Inc., Hampton, Virginia*

³*L-1 Standards and Technology, Inc., New Windsor, Maryland*

⁴*Lawrence Berkeley National Laboratory, MS 84R0171, Berkeley, California*

⁵*Scripps Institute of Oceanography, University of California, San Diego, CA, USA*



5

ABSTRACT

6 The National Institute of Standards and Technology Advanced Radiometer (NISTAR) on-
7 board Deep Space Climate Observatory (DSCOVR) provides continuous full disc global
8 broadband irradiance measurements over most of the sunlit side of the Earth. The three ac-
9 tive cavity radiometers measures the total radiant energy from the sun-lit side of the Earth in
10 shortwave (SW, 0.2-4 μm), total (0.4-100 μm), and near-infrared (NIR, 0.7-4 μm) channels.
11 The Level 1 NISTAR dataset provides the filtered radiances (the ratio between irradiance
12 and solid angle). To determine the daytime top-of-atmosphere (TOA) shortwave and long-
13 wave radiative fluxes, the NISTAR measured shortwave radiances must be unfiltered first.
14 An unfiltering algorithm was developed for the NISTAR SW and NIR channels using a spec-
15 tral radiance data base calculated for typical Earth scenes. The resulting unfiltered NISTAR
16 radiances are then converted to full disk daytime SW and LW flux, by accounting for the
17 anisotropic characteristics of the Earth-reflected and emitted radiances. The anisotropy fac-
18 tors are determined using scene identifications determined from multiple low Earth orbit and
19 geostationary satellites and the angular distribution models (ADMs) developed using data
20 collected by the Clouds and the Earth's Radiant Energy System (CERES). Global annual
21 daytime mean SW fluxes from NISTAR are about 6% greater than those from CERES, and
22 both show strong diurnal variations with daily maximum-minimum differences as great as
23 20 Wm^{-2} depending on the conditions of the sunlit portion of the Earth. They are also
24 highly correlated, having correlation coefficients of 0.89, indicating that they both capture
25 the diurnal variation. Global annual daytime mean LW fluxes from NISTAR are about 3%
26 greater than those from CERES, but the correlation between them is only about 0.38.



27 1. Introduction

28 The Earth's climate is determined by the amount and distribution of the incoming so-
29 lar radiation absorbed and the outgoing longwave radiation (OLR) emitted by the Earth.
30 Satellite observations of Earth Radiation Budget (ERB) provide critical information needed
31 to better understand the driving mechanisms of climate change; the ERB has been moni-
32 tored from space since the early satellite missions of the late 1950s and the 1960s (House
33 et al. 1986). Currently, the Clouds and the Earth's Radiant Energy System (CERES) in-
34 struments (Wielicki et al. 1996; Loeb et al. 2016) have been providing continuous global
35 top-of-atmosphere (TOA) reflected shortwave radiation and OLR since 2000. CERES data
36 have been crucial to advance our understanding of the Earth's energy balance (e.g., Tren-
37 berth et al. 2009; Kato et al. 2011; Loeb et al. 2012; Stephens et al. 2012), aerosol direct
38 radiative effects (e.g., Satheesh and Ramanathan 2000; Zhang et al. 2005; Loeb and Manalo-
39 Smith 2005; Su et al. 2013), aerosol-cloud interactions (e.g., Loeb and Schuster 2008; Quaas
40 et al. 2008; Su et al. 2010b), and to evaluate global general circulation models (e.g., Pincus
41 et al. 2008; Su et al. 2010a; Wang and Su 2013; Wild et al. 2013).

42 The Earth's radiative flux data record is augmented by the launch of the Deep Space
43 Climate Observatory (DSCOVR) on February 11, 2015. DSCOVR is designed to continu-
44 ously monitor the sunlit side of the Earth, being the first Earth-observing satellite at the
45 Lagrange-1 (L1) point, ~ 1.5 million km from Earth, where it orbits the Sun at the same rate
46 as the Earth (see Figure 1a). DSCOVR is in an elliptical Lissajous orbit around the L1 point
47 and is not positioned exactly on the Earth-sun line, therefore only about 92~97% of the sun-
48 lit Earth is visible to DSCOVR. As illustrated in Figure 1b, the daytime portion (A_h) is not
49 visible to the DSCOVR. Strictly speaking, the measurements from DSCOVR are not truly
50 'global' daytime measurements. However, for simplicity we refer to them as global daytime
51 measurements. Onboard DSCOVR, the National Institute of Standards and Technology
52 Advanced Radiometer (NISTAR) provides continuous full disc global broadband irradiance
53 measurements over most of the sunlit side of the Earth. Besides NISTAR, DSCOVR also



54 carries the Earth Polychromatic Imaging Camera (EPIC) which provides 2048 by 2048 pixel
55 imagery 10 to 22 times per day in 10 spectral bands from 317 to 780 nm. On June 8, 2015,
56 more than 100 days after launch, DSCOVR started orbiting around the L1 point.

57 The NISTAR instrument was designed to measure the global daytime shortwave (SW)
58 and longwave (LW) radiative fluxes. NISTAR measures an irradiance at the L1 point at a
59 small relative azimuth angle, ϕ_o , which varies from 4° to 15° , as shown in Figure 1a. As
60 such, the radiation it measures comes from the near-backscatter position, which is different
61 from that seen at other satellite positions as indicated in Figure 1a by the varying arrow
62 lengths corresponding to scattering angles, $\Theta_1 - \Theta_3$. Other types of Earth-orbiting satellites
63 view a given spot on the Earth from various scattering angles that vary as a function of local
64 time (e.g., geostationary) or overpass time (e.g., Sun-synchronous). When averaged over the
65 globe, the uncertainties in the anisotropy corrections are mitigated by compensation. That
66 is, any small biases at particular angles are balanced by observations taken at other angles.
67 In contrast, instruments on DSCOVR view every spot on the Earth from a single scattering
68 angle that varies slowly within a small range over the course of the Lissajous orbit. Thus, the
69 correction for anisotropy is critical. The biases in the anisotropy correction for the DSCOVR
70 scattering angle are mitigated and potentially minimized by the wide range of different scene
71 types viewed in a given NISTAR measurement.

72 Su et al. (2018) described the methodology to derive the global mean daytime shortwave
73 (SW) anisotropic factors by using the CERES angular distribution models (ADMs) and a
74 cloud property composite based on lower Earth orbiting satellite imager retrievals. These
75 SW anisotropic factors were applied to EPIC broadband SW radiances, that were estimated
76 from EPIC narrowband observations based upon narrowband-to-broadband regressions, to
77 derive the global daytime SW fluxes. Daily mean EPIC and CERES SW fluxes calculated
78 using concurrent hours agree with each other to within 2%. They concluded that the SW
79 flux agreement is within the calibration and algorithm uncertainties, which indicates that
80 the method developed to calculate the global anisotropic factors from the CERES ADMs



81 is robust and that the CERES ADMs accurately account for the Earth's anisotropy in the
82 near-backscatter direction.

83 In this paper, the same global daytime mean anisotropic factors developed by Su et al.
84 (2018) are applied to the NISTAR measurements to derive the global daytime mean SW
85 and longwave (LW) fluxes. The NISTAR data and the unfiltering algorithms developed for
86 the NISTAR shortwave and near-infrared channels are detailed in section 2. The data and
87 methodology used to derive the global daytime mean anisotropic factors are presented in
88 section 3. Hourly daytime SW and LW fluxes calculated from NISTAR measurements and
89 comparisons with the CERES Synoptic flux products (SYN1deg, Doelling et al. 2013) are
90 detailed in section 4, followed by conclusions and discussions in section 5.

91 2. NISTAR observation

92 The NISTAR instrument measures Earth irradiance data for an entire hemisphere us-
93 ing active cavity radiometers for three channels: shortwave (SW, 0.2-4.0 μm), near-infrared
94 (NIR, 0.7-4.0 μm), and total (0.2-100 μm). The NISTAR Level 1B (L1B) Earth irradiance
95 data were derived by applying an SI-traceable ground calibration, a phase sensitive demod-
96 ulation algorithm, and dark offset measurements. These irradiances are reported at the L1
97 altitude and they are divided by the solid angle (Θ) to provide the respective radiances at
98 the surface (I).

99 Filters are placed in front of the cavity radiometers to measure the energies from the SW
100 and NIR portions of the spectrum. Since no corrections for the impact of filter transmission
101 were applied to the NISTAR L1B data, the SW and NIR radiances from NISTAR must
102 first be unfiltered before they can be used to derive daytime Earth's radiative flux. Here we
103 describe an algorithm to convert measured NISTAR filtered radiances to unfiltered radiances.

104 Unfiltered SW and NIR radiances are defined as follows:

$$I_u^{band} = \int_{\lambda_1}^{\lambda_2} I_\lambda d\lambda, \quad (1)$$



105 where ‘band’ represent either SW or NIR, $\lambda(\mu m)$ is the wavelength, and I_λ ($\text{Wm}^{-2} \text{sr}^{-1}$
106 μm^{-1}) is the spectral SW radiance. The filtered radiance is the radiation that passes through
107 the spectral filter and is measured by the detector:

$$I_f^{band} = \int_{\lambda_1}^{\lambda_2} S_\lambda^{band} I_\lambda d\lambda, \quad (2)$$

108 where S_λ^{band} is the spectral transmission function. Figure 2 shows the NISTAR SW and NIR
109 spectral transmission functions. These functions are determined from ground testing done
110 in 1999 and 2010 at the National Institute of Standards and Technology (NIST).

111 Unfiltered SW and NIR radiances are determined from the filtered radiance measurements
112 as follows:

$$I_u^{sw} = a_0 + a_1(I_f^{sw}) + a_2(I_f^{sw})^2, \quad (3)$$

$$I_u^{nir} = b_0 + b_1(I_f^{nir}) + b_2(I_f^{nir})^2. \quad (4)$$

114 Here $a_0, a_1, a_2, b_0, b_1,$ and b_2 are theoretically derived regression coefficients that depend on
115 scene type and Sun-viewing geometry. They are determined from a regression analysis of
116 theoretically derived filtered and unfiltered radiances simulated for typical Earth scenes and
117 the spectral transmission functions shown in Figure 2.

118 The spectral radiance database is calculated using high-spectral-resolution radiative trans-
119 fer model (Kato et al. 2002). Unfiltered radiances are determined by integrating spectral
120 radiances over the appropriate wavelength intervals using Gaussian quadrature. Similarly,
121 filtered radiances are computed by integrating over the product of spectral radiance and
122 spectral transmission function. The regression coefficients are derived at 480 angles: 6 so-
123 lar zenith angles (0.0, 29.0, 41.4, 60.0, 75.5, 85.0 degrees), 8 viewing zenith angles (0, 12,
124 24, 36, 48, 60, 72, 84 degrees), and 10 relative azimuth angles (0 to 180, at every 20 de-
125 grees). For angles between those given above, the regression coefficients are derived by linear
126 interpolation.

127 The database includes spectral radiances calculated over ocean, land/desert, snow/ice
128 surfaces for clear and cloudy conditions. Table 1 summarizes the cases that are included in



129 the database, there are a total of 722 clear-sky cases and a total of 1519 cloudy-sky cases
130 for each Sun-viewing geometry. Regression coefficients are derived based upon the simulated
131 radiances in this database separately for clear and cloudy conditions for ocean, land/desert,
132 and snow/ice for each Sun-viewing geometry.

133 The ratio, κ , between filtered and unfiltered radiances is calculated for SW and NIR
134 bands. Table 2 lists the mean and the standard deviation of the ratios at different solar
135 zenith angles. The ratios for the SW band are extremely stable, varying less than 0.3%
136 among the scenes and Sun-viewing geometries considered. However, the variability in the
137 ratios of the NIR band can be as large as 6%. As the NISTAR view always contains clouds,
138 we choose to use the mean ratios of the cloudy ocean and land cases in Table 2, which
139 is 0.8690 for the SW band. The estimated uncertainty for the SW band caused by the
140 unfiltering process is less than 0.1%. The mean ratio for the NIR band is 0.8583, and the
141 unfiltering uncertainty can be as large as 1~2%. These mean ratios of the SW and NIR
142 bands are used to convert the filtered radiances to unfiltered radiances:

$$I_u^{sw} = \frac{I_f^{sw}}{\kappa^{sw}}, \quad (5)$$

143

$$I_u^{nir} = \frac{I_f^{nir}}{\kappa^{nir}}. \quad (6)$$

144 Here I_f^{sw} and I_f^{nir} are the filtered radiances directly from the NISTAR L1B data. As there
145 is no filter placed in front of the total channel, the radiance from the total channel does
146 not need to be unfiltered. The LW (4-100 μm) radiance can be derived by subtracting the
147 unfiltered SW radiance from the total:

$$I_u^{lw} = I^{tot} - I_u^{sw}, \quad (7)$$

148 The unfiltered radiances (I_u^{sw} , I_u^{lw} , and I_u^{nir}) will be used hereafter to derive the daytime
149 mean radiative flux. Although NISTAR L1B data provide observations every second, hourly
150 data (smoothed with 4-hour running mean) are used to derive fluxes because of the level of
151 noise presented in the measurements (DSCOVER NISTAR data quality report v02).



152 3. Global daytime shortwave and longwave anisotropic 153 factors

154 To derive the global daytime mean SW and LW fluxes from the NISTAR unfiltered
155 radiances, the anisotropy of the TOA radiance field must be considered. The CERES Edition
156 4 empirical ADMs and a cloud property composite based upon lower Earth orbit satellite
157 retrievals are used here to estimate the global mean shortwave and longwave anisotropic
158 factors.

159 *a. CERES ADMs*

160 The Edition 4 CERES ADMs (Su et al. 2015) are constructed using the CERES ob-
161 servations taken during the rotating azimuth plane (RAP) scan mode. In this mode, the
162 instrument scans in elevation as it rotates in azimuth, thus acquiring radiance measurements
163 from a wide range of viewing combinations. The CERES ADMs are derived for various scene
164 types, which are defined using a combination of variables (e.g., surface type, cloud fraction,
165 cloud optical depth, cloud phase, aerosol optical depth, precipitable water, lapse rate, etc).
166 To provide accurate scene type information within CERES footprints, imager (Moderate
167 Resolution Imaging Spectroradiometer (MODIS) on *Terra* and *Aqua*) cloud and aerosol re-
168 trievals (Minnis et al. 2010, 2011) are averaged over CERES footprints by accounting for
169 the CERES point spread function (PSF, Smith 1994) and are used for scene type classifica-
170 tion. Over a given scene type (χ), the CERES measured radiances are sorted into discrete
171 angular bins. Averaged radiances (\hat{I}) in all angular bins are calculated and all radiances in
172 the upwelling directions are integrated to provide the ADM flux (\hat{F}). The ADM anisotropic
173 factors (R) for scene type χ are then calculated as:

$$R(\theta_0, \theta, \phi, \chi) = \frac{\pi \hat{I}(\theta_0, \theta, \phi, \chi)}{\int_0^{2\pi} \int_0^{\frac{\pi}{2}} \hat{I}(\theta_0, \theta, \phi, \chi) \cos\theta \sin\theta d\theta d\phi} = \frac{\pi \hat{I}(\theta_0, \theta, \phi, \chi)}{\hat{F}(\theta_0, \chi)}, \quad (8)$$



174 where θ_0 is the solar zenith angle, θ is the CERES viewing zenith angle, and ϕ is the relative
175 azimuth angle between CERES and the solar plane.

176 *b. EPIC composite data*

177 As stated in the section above, anisotropy of the radiation field at the TOA was con-
178 structed for different scene types, which were defined using many variables including cloud
179 properties such as cloud fraction, cloud optical depth, and cloud phase (Loeb et al. 2005;
180 Su et al. 2015). Although the EPIC L2 cloud product includes threshold-based cloud mask,
181 which identifies the EPIC pixels as high confident clear, low confident clear, high confident
182 cloudy, and low confident cloudy (Yang et al. 2018), the low resolution of EPIC imagery
183 ($24 \times 24 \text{ km}^2$) and its lack of infrared channels diminish its capability to identify clouds and
184 to accurately retrieve cloud properties. As EPIC lacks the channels that are suitable for
185 cloud size and phase retrievals (Meyer et al. 2016), two cloud optical depths are determined
186 assuming the cloud phase is liquid or ice using constant cloud effective radius ($14 \mu\text{m}$ for
187 liquid and $30 \mu\text{m}$ for ice) for cloudy EPIC pixels. These cloud properties are not sufficient
188 to provide the scene type information necessary for ADM selections. Therefore, more accu-
189 rate cloud property retrievals are needed to provide anisotropy characterizations to convert
190 radiances to fluxes.

191 To accomplish this, we take advantage of the cloud property retrievals from multiple im-
192 agers on low Earth orbit (LEO) satellites and geostationary (GEO) satellites. The LEO satel-
193 lite imagers include the MODerate-resolution Imaging Spectroradiometer (MODIS) on the
194 Terra and Aqua satellites, the Visible Infrared Imaging Suite (VIIRS) on the Suomi-National
195 Polar-orbiting Partnership satellite, and the Advanced Very High Resolution Radiometer
196 (AVHRR) on the NOAA and MetOps platforms. The GEO imagers are on the Geostation-
197 ary Operational Environmental Satellites (GOES), the Meteosat series, and Himawari-8 to
198 provide semi-global coverage. All cloud properties were determined using a common set of
199 algorithms, the Satellite Cloud and Radiation Property retrieval System (SatCORPS, Min-



200 nis et al. 2008b, 2016), based on the CERES cloud detection and retrieval system (Minnis
201 et al. 2008a, 2010, 2011). Cloud properties from these LEO/GEO imagers are optimally
202 merged together to provide a seamless global composite product at 5-km resolution by us-
203 ing an aggregated rating that considers five parameters (nominal satellite resolution, pixel
204 time relative to the EPIC observation time, viewing zenith angle, distance from day/night
205 terminator, and sun glint factor to minimize the usage of data taken in the glint region) and
206 selects the best observation at the time nearest to the EPIC measurements. About 80% of the
207 LEO/GEO satellite overpass times are within 40 minutes of the EPIC measurements, while
208 96% are within two hours of the EPIC measurements. Most of the regions covered by GEO
209 satellites (between around 50°S and 50°N) have a very small time difference, in the range
210 of ± 30 minutes, because the availability of hourly GEO observations. The polar regions are
211 also covered very well by polar orbiters. Thus, larger time differences are generally occurred
212 over the 50° to 70° latitude regions. Given the temporal resolution of the currently available
213 GEO/LEO satellites, this is the best collocation possible for those latitudes. The global
214 composite data are then remapped into the EPIC FOV by convolving the high-resolution
215 cloud properties with the EPIC point spread function (PSF) defined with a half-pixel ac-
216 curacy to produce the EPIC composite. As the PSF is sampled with half-pixel accuracy,
217 the nominal spacing of the PSF grid is about the same size as in the global composite data.
218 Thus, the accuracy of the cloud fraction in the EPIC composite is not degraded compared
219 to the global composite (Khlopenkov et al. 2017). PSF-weighted averages of radiances and
220 cloud properties are computed separately for each cloud phase, because the LEO/GEO cloud
221 products are retrieved separately for liquid and ice clouds (Minnis et al. 2008b). Ancillary
222 data (i.e. surface type, snow and ice map, skin temperature, precipitable water, etc.) needed
223 for anisotropic factor selections are also included in the EPIC composite. These composite
224 images are produced for each observation time of the EPIC instrument (typically 300 to 600
225 composites per month). Detailed descriptions of the method and the input used to generate
226 the global and EPIC composites are provided in Khlopenkov et al. (2017).



227 Figure 3(a) shows an image from EPIC taken on May 15, 2017 at 12:17 UTC, the cor-
228 responding total cloud fraction (the sum of liquid and ice cloud fractions) from the EPIC
229 composite is shown in 3(b). The liquid and ice cloud fraction, optical depth, and effective
230 height are shown in Figure 3(c-h). For this case, most of the clouds are in the liquid phase.
231 Optically thick liquid clouds with effective heights of 2 to 4 km are observed in the northern
232 Atlantic ocean and in the Arctic. Ice clouds with effective heights of 8 to 10 km are observed
233 off the west coast of Africa and Europe.

234 *c. Calculating global daytime anisotropic factors*

235 To determine the global daytime mean anisotropic factors, we use the anisotropies char-
236 acterized in the CERES ADMs and they are selected based upon the scene type information
237 provided by the EPIC composite for every EPIC FOV. For a given EPIC FOV (j), its
238 anisotropic factor is determined based upon the Sun-EPIC viewing geometry and the scene
239 identification information provided by the EPIC composite:

$$R_j(\theta_0, \theta^e, \phi^e, \chi^e) = \frac{\pi \hat{I}_j(\theta_0, \theta^e, \phi^e, \chi^e)}{\hat{F}_j(\theta_0, \chi^e)}, \quad (9)$$

240 where θ^e is the EPIC viewing zenith angle, ϕ^e is the relative azimuth angle between EPIC
241 and the solar plane, and χ^e is the scene identification from the EPIC composite. To derive
242 the global mean anisotropic factor, we follow the method developed by Su et al. (2018) and
243 calculate the global daytime mean ADM radiance as:

$$\bar{I} = \frac{\sum_{j=1}^N \hat{I}_j(\theta_0, \theta^e, \phi^e, \chi^e)}{N}. \quad (10)$$

244 To calculate the global mean ADM flux, we first grid the ADM flux (\hat{F}) for each EPIC
245 pixel into 1° latitude by 1° longitude bins ($\hat{F}(\text{lat}, \text{lon})$). These gridded ADM fluxes are then
246 weighted by *cosine* of latitude to provide the global daytime mean ADM flux:

$$\bar{F} = \frac{\sum_{j=1}^M \hat{F}_j(\text{lat}, \text{lon}) \cos(\text{lat}_j)}{\sum \cos(\text{lat}_j)}. \quad (11)$$



247 The global mean anisotropic factor is calculated as:

$$\bar{R} = \frac{\pi \hat{I}}{\hat{F}}. \quad (12)$$

248 We use $\overline{R_{sw}}$ and $\overline{R_{lw}}$ to denote the mean SW and LW anisotropic factors. The mean SW
249 anisotropic factor is then used to convert the NISTAR SW unfiltered radiance to flux:

$$F_n^{sw} = \frac{\pi I_u^{sw}}{R_{sw}}. \quad (13)$$

250 The LW flux is similarly derived from the following:

$$F_n^{lw} = \frac{\pi I_u^{lw}}{R_{lw}}. \quad (14)$$

251 Figure 4 shows an example of SW and LW anisotropic factors for every EPIC FOV. The
252 SW anisotropic factors are generally smaller over clear than over cloudy oceanic regions.
253 Over land, however, the SW anisotropic factors are larger over clear regions than over cloudy
254 regions because of the hot spot effect, which leads to anisotropic factors greater than 1.6
255 over clear land regions at large viewing zenith angles. The LW anisotropic factors show
256 much less variability compare to the SW anisotropic factors, with limb darkening being the
257 dominate feature. The mean SW and LW anisotropic factors for this case are 1.275 and
258 1.041, respectively.

259 4. NISTAR shortwave and longwave flux

260 The temporal resolution of the NISTAR Level 1B data is one second, however, mean-
261 ingful changes in the data only occur over several shutter cycles due to the demodulation
262 algorithm, which includes a box car averaging filter. Following demodulation, significant
263 instrument noise remains. Therefore, further averaging in time over a minimum of 2 hours
264 is recommended to further reduce noise levels ([https://eosweb.larc.nasa.gov/project/dscovr](https://eosweb.larc.nasa.gov/project/dscovr/DSCOVN_NISTAR_Data_Quality_Report_V02.pdf)
265 [/DSCOVN_NISTAR_Data_Quality_Report_V02.pdf](https://eosweb.larc.nasa.gov/project/dscovr/DSCOVN_NISTAR_Data_Quality_Report_V02.pdf)). In this study, we use hourly radiances
266 averaged from 4-hour running means as suggested by the NISTAR instrument team. The



267 hours that are coincident with the EPIC image times are converted to fluxes using the
268 global anisotropic factors calculated from the EPIC composites. Figure 5 shows the hourly
269 SW and LW fluxes derived from NISTAR for April (a) and July (b) 2017. For both months,
270 the SW fluxes fluctuate around 210 Wm^{-2} , with the difference between daily maximum and
271 minimum as large as 30 Wm^{-2} . The LW fluxes fluctuate around 260 Wm^{-2} , and exhibit
272 surprisingly large diurnal variations.

273 These NISTAR fluxes are compared to the CERES Synoptic radiative fluxes and clouds
274 product (SYN1deg, Doelling et al. 2013), which provides hourly cloud properties and fluxes
275 for each 1° latitude by 1° longitude. Within the SYN1deg data product, fluxes between
276 CERES observations are inferred from hourly GEO visible and infrared imager measure-
277 ments between 60°S and 60°N using observation-based narrowband-to-broadband radiance
278 and radiance-to-flux conversion algorithms. However, the GEO narrowband channels have
279 a greater calibration uncertainty than MODIS and CERES. Several procedures are imple-
280 mented to ensure the consistency between the MODIS-derived and GEO-derived cloud prop-
281 erties, and between the CERES fluxes and the GEO-based fluxes. These include calibrating
282 GEO visible radiances against the well-calibrated MODIS $0.65 \mu\text{m}$ radiances by ray-matching
283 MODIS and GEO radiances; applying similar cloud retrieval algorithms to derive cloud prop-
284 erties from MODIS and GEO observations; and normalizing GEO-based broadband fluxes
285 to CERES fluxes using coincident measurements. Comparisons with broadband fluxes from
286 Geostationary Earth Radiation Budget (GERB, Harries et al. 2005) indicate that SYN1deg
287 hourly fluxes are able to capture the subtle diurnal flux variations. Comparing with the
288 GERB fluxes, the bias of the SYN SW fluxes is 1.3 Wm^{-2} , the monthly regional all-sky SW
289 flux RMS error is 3.5 W m^{-2} , and the daily regional all-sky SW flux RMS error is 7.8 W m^{-2}
290 (Doelling et al. 2013). These uncertainties could be overestimated, as the GERB domain
291 has a disproportionate number of strong diurnal cycle regions as compared with the globe.

292 To account for the missing energy from the daytime portion that is not observed by the
293 NISTAR (A_h in Figure 1b), the hourly gridded SYN fluxes are integrated by considering



294 only the grid boxes that are visible to NISTAR to produce the global mean daytime fluxes
295 that are comparable to those from the NISTAR measurements:

$$\overline{F_{syn}} = \frac{\sum F_j \cos(lat_j) \omega_j}{\sum \cos(lat_j) \omega_j}. \quad (15)$$

296 Here F_j is the gridded hourly CERES SYN fluxes, lat is the latitude, and ω indicates whether
297 a grid box is visible to NISTAR (=1 when visible, =0 when not visible). Figure 6a) shows
298 an example of the gridded SYN SW fluxes at 10 UTC on January 1, 2017. SW fluxes
299 for the daytime grid boxes are shown in color, while all nighttime grid boxes are shown in
300 white. Figure 6b) shows the area (in red) visible to the NISTAR view, daytime areas of
301 Scandinavian and South America are not within the NISTAR view and are therefore not
302 included in the comparison with the NISTAR fluxes.

303 Figure 7 compares the SW fluxes from NISTAR with those from CERES SYN1deg
304 product integrated for the NISTAR view (Eq. 19) for April (a) and July (b) 2017. The
305 CERES SW fluxes oscillate around 200 Wm^{-2} and 195 Wm^{-2} for April and July, whereas
306 the NISTAR counterparts are about 10 to 20 Wm^{-2} greater. The maxima and minima of
307 SW fluxes from NISTAR align well with those from CERES, though the differences between
308 daily maximum and minimum from NISTAR appear to be larger than those from CERES.
309 The diurnal variations of SW flux derived from EPIC showed a much better agreement with
310 those from CERES (Su et al. 2018). The exact cause for these larger diurnal variations
311 from NISTAR SW flux is not known and could be due to onboard data processing. LW
312 flux comparisons are shown in Figure 8. The daily maximum-minimum LW differences from
313 CERES are typically less than 15 Wm^{-2} and exhibit small day-to-day and month-to-month
314 variation. However, the daily maximum-minimum LW differences from NISTAR can vary
315 from 10 Wm^{-2} to 50 Wm^{-2} . These larger than expected variability of NISTAR LW fluxes
316 are due to the fact that noise and offset variabilities from both the NISTAR total and SW
317 channel are present in the NISTAR LW radiances. The NISTAR LW fluxes are consistently
318 greater than CERES LW fluxes by about 10 to 20 Wm^{-2} in April. The LW fluxes agree
319 better for July, but the NISTAR LW fluxes show larger diurnal variations than the CERES



320 fluxes.

321 Figure 9 compares the SW and LW fluxes from CERES SYN1deg product with those
322 from NISTAR at all coincident hours of 2017. The mean SW fluxes are 204.5 Wm^{-2} and
323 217.2 Wm^{-2} , respectively, for CERES and NISTAR, and the RMS error is 14.1 Wm^{-2} (Fig-
324 ure 9a). The mean LW fluxes are 246.4 Wm^{-2} and 252.8 Wm^{-2} for CERES and NISTAR,
325 and the RMS error is 10.3 Wm^{-2} (Figure 9b). Tables 3 and 4 summarize the flux com-
326 parisons between NISTAR and CERES for all months of 2017. The NISTAR SW fluxes
327 are consistently greater than those from CERES SYN1deg by about 3.4% to 7.8%, and the
328 NISTAR LW fluxes are also greater than those from CERES SYN1deg by 1.0% to 5.0%.
329 Furthermore, the SW fluxes from NISTAR are highly correlated (correlation coefficient of
330 about 0.89) with those from CERES SYN1deg, but the correlation for the LW fluxes are
331 rather low (correlation coefficient of about 0.38).

332 NISTAR fluxes derived at the EPIC image times are averaged into daily means and are
333 compared with the daily means from CERES SYN1deg using concurrent hours (Figure 10).
334 The NISTAR SW fluxes are consistently higher than those from CERES by about 10 to 15
335 Wm^{-2} . CERES SW fluxes show a strong annual cycle, which is driven by the incident solar
336 radiation that is affected by the Earth-Sun distance. This annual cycle is also evident in the
337 NISTAR SW fluxes, albeit the fluxes during the period from April to August are flatter than
338 those from CERES. The NISTAR LW fluxes are greater than those from CERES except
339 during the boreal summer months, with the largest difference of 10 Wm^{-2} in February and
340 the smallest difference of a few Wm^{-2} during the boreal summer months. The CERES LW
341 fluxes show an annual cycle of about 10 Wm^{-2} , with the largest LW fluxes occurring during
342 the boreal summer when the vast land masses of the northern hemisphere are warmer than
343 during the other seasons. The annual cycle of the NISTAR LW fluxes shows less seasonal
344 variation. From April to October, the NISTAR LW fluxes oscillate around 255 Wm^{-2} , and
345 oscillate around 250 Wm^{-2} for other months. Additionally, the CERES LW fluxes exhibit
346 much smaller day-to-day variations than their NISTAR counterparts. Note some of the



347 variations of daily mean fluxes shown in Figure 10 are due to temporal sampling changes
348 when data transmissions encountered difficulties and/or during spacecraft maneuvers.

349 5. Conclusions and discussions

350 The SW radiances included in the NISTAR L1B data are filtered radiances and the effect
351 of the filter transmission must be addressed before these measurements can be used to derive
352 any meaningful fluxes. A comprehensive spectral radiance database has been developed
353 to investigate the relationship between filtered and unfiltered radiances using theoretically
354 derived values simulated for typical Earth scenes and the NISTAR spectral transmission
355 functions. The ratio between filtered and unfiltered SW radiances is very stable, varying
356 less than 0.3% for the scenes and the Sun-viewing geometries included in the database. The
357 mean ratio of 0.8690 is used to derive the unfiltered SW radiance from the NISTAR L1B
358 filtered SW radiance measurements.

359 To convert these unfiltered radiances into fluxes, the anisotropy of the radiance field must
360 be taken into account. We use the scene-type dependent CERES angular distribution models
361 to characterize the global SW and LW anisotropy. These global anisotropies are calculated
362 based upon the anisotropies for each EPIC pixel. To accurately account for the anisotropy for
363 each EPIC pixel, an EPIC composite was developed which includes all information needed
364 for angular distribution model selections. The EPIC composite includes cloud property
365 retrievals from multiple imagers on LEO and GEO satellites. Cloud properties from these
366 LEO and GEO imagers are optimally merged together to provide a global composite product
367 at 5-km resolution by using an aggregated rating that considers several factors and selects the
368 best observation at the time nearest to the EPIC measurements. The global composite data
369 are then remapped into the EPIC FOV by convolving the high-resolution cloud properties
370 with the EPIC PSF to produce the EPIC composite. PSF-weighted averages of radiances
371 and cloud properties are computed separately for each cloud phase, and ancillary data needed



372 for anisotropic factor selections are also included in the EPIC composite.

373 These global anisotropies are applied to the NISTAR radiances to produce the global
374 daytime SW and LW fluxes and they are validated against the CERES Synoptic 1° latitude
375 by 1° longitude flux product. Only the grid boxes that are visible to the NISTAR view
376 are integrated to produce the global mean daytime fluxes that are comparable to the fluxes
377 from the NISTAR measurements. The NISTAR SW fluxes are consistently greater than
378 those from CERES SYN1deg by 10 Wm^{-2} to 15 Wm^{-2} (3.3% to 7.8%), but these two SW
379 flux datasets are highly correlated indicating that the diurnal and seasonal variations of
380 the SW fluxes are fairly similar for both of them. The NISTAR LW fluxes are also greater
381 than those from CERES SYN1deg, but the magnitude of the difference has larger month-
382 to-month variations than that for the SW fluxes. The largest difference of about 10 Wm^{-2}
383 ($\sim 9\%$) occurred in January 2017 and the smallest difference of about $\sim 2 \text{ Wm}^{-2}$ ($\sim 1\%$)
384 occurred during the boreal summer months. Furthermore, the NISTAR LW fluxes have very
385 low correlations with the CERES LW fluxes. NISTAR LW fluxes exhibit a nearly flat annual
386 variation, whereas the CERES LW fluxes exhibit a distinct annual cycle with the highest
387 LW flux occurs in July when the vast northern hemisphere land masses are warmest. The
388 NISTAR LW fluxes also exhibit unrealistically large day-to-day variations.

389 The SW flux discrepancy between NISTAR and CERES is caused by: 1) CERES instru-
390 ment calibration uncertainty, 2) CERES flux algorithm uncertainty, 3) NISTAR instrument
391 measurement uncertainty, and 4) NISTAR flux algorithm uncertainty. The CERES SW chan-
392 nel calibration uncertainty is 1% (Loeb et al. 2018), which corresponds to about 2.1 Wm^{-2}
393 for daytime mean SW fluxes. The CERES algorithm uncertainty includes radiance-to-flux
394 conversion error, which is 1.0 Wm^{-2} according to Su et al. (2015), and diurnal correction un-
395 certainty, which is estimated to be 1.9 Wm^{-2} when Terra and Aqua are combined (Loeb et al.
396 2018). The NISTAR SW channel measurement uncertainty is 2.1%, which corresponds to
397 4.4 Wm^{-2} . The NISTAR algorithm uncertainty is essentially the radiance-to-flux conversion
398 error. The estimation of this error source is not readily available given the unique NISTAR



399 viewing perspective. However, if we assume the discrepancy between EPIC derived SW flux
400 and CERES SW flux (Su et al. 2018) is also from uncertainty sources 1) and 2) listed above,
401 plus the EPIC calibration, narrowband-to-broadband conversion, and radiance-to-flux con-
402 version for EPIC, then we can deduce that the radiance-to-flux conversion uncertainty for
403 the NISTAR viewing geometry should be less than 2 Wm^{-2} . Thus the total difference ex-
404 pected from these uncertainty sources should be $(2.1^2 + 1.9^2 + 1.0^2 + 4.4^2 + 2.0^2)^{1/2} = 5.7$
405 Wm^{-2} .

406 Similarly, the LW flux discrepancy between NISTAR and CERES is due to the same
407 sources of error. The CERES LW channel calibration uncertainty is 1.8 Wm^{-2} . The CERES
408 LW radiance-to-flux conversion error is about 0.75 Wm^{-2} (Su et al. 2015), and diurnal cor-
409 rection uncertainty is estimated to be 2.2 Wm^{-2} (Loeb et al. 2018). However, the CERES
410 LW ADMs were developed without taking the relative azimuth angle into consideration,
411 which has little impact on the CERES LW flux accuracy because of its Sun-synchronous
412 orbit. Given that the NISTAR only views the Earth from the backscattering angles, the LW
413 flux uncertainty due to radiance-to-flux conversion could be larger for the clear-sky foot-
414 prints (Minnis et al. 2004). As the clear-sky occurrences are small at the EPIC footprint
415 size level, our best guesstimate of this uncertainty is no more than 0.4 Wm^{-2} . The cali-
416 bration uncertainty for NISTAR LW is deduced from the calibration uncertainties of total
417 and SW channels. The total channel calibration uncertainty is 1.5%, which is about 6.8
418 Wm^{-2} assuming the total radiative energy of 450 Wm^{-2} . The SW channel measurement
419 uncertainty is 4.4 Wm^{-2} . The resulting LW channel measurement uncertainty is thus equal
420 to $(6.8^2 + 4.4^2)^{1/2} = 8.1 \text{ Wm}^{-2}$. Although no direct estimation of the radiance-to-flux con-
421 version uncertainty for LW is available, we do not expect that it exceeds its SW counterpart
422 of 2.0 Wm^{-2} . Thus the total difference expected from these uncertainty sources should be
423 $(1.8^2 + 0.75^2 + 0.4^2 + 2.2^2 + 8.1^2 + 2.0^2)^{1/2} = 8.9 \text{ Wm}^{-2}$.

424 The uncertainty sources listed above can explain part of the SW flux differences and
425 all of the LW flux differences between CERES and NISTAR. The error sources related to



426 NISTAR are preliminary and are under careful evaluation. Although the LW flux differences
427 between CERES and NISTAR are within the uncertainty estimation, the correlation between
428 NISTAR and CERES is rather low, about 0.38. This is because the NISTAR LW radiance
429 is derived as the difference between total channel radiance and SW channel radiance, thus
430 noise and offset variability of both the NISTAR total and SW channels are present in the
431 NISTAR LW fluxes. As a result, more variability is expected in the LW data which leads
432 to the low correlation. The diurnal variations of the SW and LW fluxes from both NISTAR
433 and CERES SYN1deg will be compared with the high-temporal resolution model outputs
434 from the Coupled Model Intercomparison Project.

435 *Acknowledgments.*

436 This research was supported by the NASA DSCOVR project. The CERES data were
437 obtained from the NASA Langley Atmospheric Science Data Center at
438 [https://eosweb.larc.nasa.gov/project/ceres/ssf_terra-fm1_ed4a_table\(ssf_aqua-fm3_ed4a_table\)](https://eosweb.larc.nasa.gov/project/ceres/ssf_terra-fm1_ed4a_table(ssf_aqua-fm3_ed4a_table)).
439 The data used to produce the figures and tables in this paper are available to readers upon
440 request. We thank Szedung Sun-Mack, Rabindra Palikonda, and Kristopher Bedka for pro-
441 cessing the LEO/GEO data used to construct the EPIC composite.



442

443

REFERENCES

444 Doelling, D. R., N. G. Loeb, D. F. Keyes, M. L. Nordeen, D. Morstad, B. A. Wielicki, D. F.
445 Young, and M. Sun, 2013: Geostationary enhanced temporal interpolation for CERES flux
446 products. *J. Atmos. Oceanic Technol.*, **30**, 1072–1090, doi:10.1175/JTECH-D-12-00136.1.

447 Harries, J. E., J. E. Russell, J. A. Hanafin, H. Brindley, J. Futyran, J. Rufus, and coauthors,
448 2005: The geostationary earth radiation budget project. *Bull. Am. Meteor. Soc.*, **86**, 945–
449 960.

450 House, F. B., A. Gruber, G. E. Hunt, and A. T. Mecherikunnel, 1986: History of satellite
451 missions and measurements of the Earth radiation budget (1957-1984). *Rev. Geophys.*, **24**,
452 357–377.

453 Kato, S., N. G. Loeb, and K. Rutledge, 2002: Estimate of top-of-atmosphere albedo for a
454 molecular atmosphere over ocean using Clouds and the Earth’s Radiant Energy System
455 measurements. *J. Geophys. Res.*, **107** (D19), doi:10.1029/2001JD001309.

456 Kato, S., et al., 2011: Improvements of top-of-atmosphere and surface irradiance computa-
457 tion with CALIPSO-, and MODIS-derived cloud and aerosol properties. *J. Geophys. Res.*,
458 **116** (D19209), D19 209, doi:10.1029/2011JD016050.

459 Khlopenkov, K., D. Duda, M. Thieman, P. Minnis, W. Su, and K. Bedka, 2017: Devel-
460 opment of multi-sensor global cloud and radiance composites for Earth radiation budget
461 monitoring from DSCOVR. *Remote sensing of clouds and the atmosphere XXII*, A. Com-
462 eron, E. I. Kassianov, K. Schafer, R. H. Picard, and K. Weber, Eds., Warsaw, Poland,
463 Proc. SPIE 10424, Vol. 10424K (2 October 2017), doi:10.1117/12.2278645.

464 Loeb, N. G., S. Kato, K. Loukachine, and N. Manalo-Smith, 2005: Angular distribution
465 models for top-of-atmosphere radiative flux estimation from the clouds and the earth’s



- 466 radiant energy system instrument on the terra satellite. part I: Methodology. *J. Atmos.*
467 *Oceanic Technol.*, **22**, 338–351.
- 468 Loeb, N. G., J. M. Lyman, G. C. Johnson, R. P. Allan, D. R. Doelling, T. Wong, B. J.
469 Soden, and G. L. Stephens, 2012: Observed changes in top-of-the-atmosphere radiation
470 and upper-ocean heating consistent within uncertainty. *Nature Geosci.*, **5**, 110–113, doi:
471 10.1038/NGEO1375.
- 472 Loeb, N. G. and N. Manalo-Smith, 2005: Top-of-atmosphere direct radiative effect of aerosols
473 over global oceans from merged CERES and MODIS observations. *J. Climate*, **18**, 3506–
474 3526.
- 475 Loeb, N. G., N. Manalo-Smith, W. Su, M. Shankar, and S. Thomas, 2016: CERES top-of-
476 atmosphere Earth radiation budget climate data record: Accounting for in-orbit changes
477 in instrument calibration. *Remote Sens.*, **8** (182), doi:10.3390/rs8030182.
- 478 Loeb, N. G. and G. L. Schuster, 2008: An observational study of the relationship between
479 cloud, aerosol and meteorology in broken low-level cloud conditions. *J. Geophys. Res.*,
480 **113** (D14214), D14 214, doi:10.1029/2007JD009763.
- 481 Loeb, N. G., et al., 2018: Clouds and the Earth’s Radiant Energy System (CERES) Energy
482 Balanced and Filled (EBAF) Top-of-Atmosphere (TOA) Edition-4.0 Data Product. *J.*
483 *Climate*, **31**, 895–918, doi:10.1175/JCLI-D-17-0208.1.
- 484 Meyer, K., Y. Yang, and S. Platnick, 2016: Uncertainties in cloud phase and optical thickness
485 retrievals from the Earth Polychromatic Imaging Camera (EPIC). *Atmos. Meas. Tech.*, **9**,
486 1785–1797, doi:10.5194/amt-9-1785-2016.
- 487 Minnis, P., K. Bedka, Q. Z. Trepte, C. R. Yost, S. T. Bedka, B. Scarino, K. V. Khlopenkov,
488 and M. M. Khaiyer, 2016: *A consistent long-term cloud and clear-sky radiation property*
489 *dataset from the Advanced Very High Resolution Radiometer (AVHRR)*. *Climate Algo-*



- 490 *rhythm Theoretical Basis Document (C-ATBD)*. CDRP-ATBD-0826 Rev 1–NASA,NOAA
491 CDR Program, doi:10.7289/V5HT2M8T.
- 492 Minnis, P., A. V. Gambheer, and D. R. Doelling, 2004: Azimuthal anisotropy of longwave and
493 infrared window radiances from the Clouds and the Earth’s Radiant Energy System on the
494 Tropical Rainfall Measuring Mission on Terra satellites. *J. Geophys. Res.*, **109 (D08202)**,
495 doi:10.1029/2003JD004471.
- 496 Minnis, P., et al., 2008a: Cloud detection in nonpolar regions for CERES using TRMM VIRS
497 and TERRA and AQUA MODIS data. *IEEE Trans. Geosci. Remote Sensing*, **46 (11)**,
498 3857–3884.
- 499 Minnis, P., et al., 2008b: Near-real time cloud retrievals from operational and research
500 meteorological satellites. *Proc. SPIE 7108, Remote Sens. Clouds Atmos. XIII*, Cardiff,
501 Wales, UK, doi:10.1117/12.800344.
- 502 Minnis, P., et al., 2010: CERES Edition 3 cloud retrievals. *13th Conference on Atmospheric*
503 *Radiation*, Am. Meteorol. Soc., Oregon, Portland.
- 504 Minnis, P., et al., 2011: CERES Edition-2 cloud property retrievals using TRMM VIRS
505 and TERRA and AQUA MODIS data, Part I: Algorithms. *IEEE Trans. Geosci. Remote*
506 *Sensing*, **49 (11)**, 4374–4400, doi:10.1109/TGRS.2011.2144601.
- 507 Pincus, R., C. P. Batstone, R. J. P. Hofmann, K. E. Taylor, and P. J. Glecker, 2008: Evalu-
508 ating the present-day simulation of clouds, precipitation, and radiation in climate models.
509 *J. Geophys. Res.*, **113 (D14209)**, D14 209, doi:10.1029/2007JD009334.
- 510 Quaas, J., O. Boucher, N. Bellouin, and S. Kinne, 2008: Satellite-based estimate of the
511 direct and indirect aerosol climate forcing. *J. Geophys. Res.*, **113 (D05204)**, D05 204,
512 doi:10.1029/2007JD008962.



- 513 Satheesh, S. K. and V. Ramanathan, 2000: Large differences in tropical aerosol forcing at
514 the top of the atmosphere and earth's surface. *Nature*, **405**, 60–63.
- 515 Smith, G. L., 1994: Effects of time response on the point spread function of a scanning
516 radiometer. *Appl. Opt.*, **33**, 7031–7037.
- 517 Stephens, G. L., et al., 2012: An update on Earth's energy balance in light of the latest
518 global observations. *Nature Geosci.*, **5**, 691–696, doi:10.1038/NCEO1580.
- 519 Su, W., A. Bodas-Salcedo, K.-M. Xu, and T. P. Charlock, 2010a: Comparison of the trop-
520 ical radiative flux and cloud radiative effect profiles in a climate model with Clouds and
521 the Earth's Radiant Energy System (CERES) data. *J. Geophys. Res.*, **115** (D01105),
522 D01105, doi:10.1029/2009JD012490.
- 523 Su, W., J. Corbett, Z. A. Eitzen, and L. Liang, 2015: Next-generation angular distribution
524 models for top-of-atmosphere radiative flux calculation from the CERES instruments:
525 Methodology. *Atmos. Meas. Tech.*, **8**, 611–632, doi:10.5194/amt-8-611-2015.
- 526 Su, W., N. G. Loeb, G. L. Schuster, M. Chin, and F. G. Rose, 2013: Global all-sky shortwave
527 direct radiative forcing of anthropogenic aerosols from combined satellite observations and
528 GOCART simulations. *J. Geophys. Res.*, **118**, 1–15, doi:10.1029/2012JD018294.
- 529 Su, W., N. G. Loeb, K. Xu, G. L. Schuster, and Z. A. Eitzen, 2010b: An estimate of aerosol
530 indirect effect from satellite measurements with concurrent meteorological analysis. *J.*
531 *Geophys. Res.*, **115** (D18219), D18219, doi:10.1029/2010JD013948.
- 532 Su, W., et al., 2018: Determining the shortwave radiative flux from Earth Polychromatic
533 Imaging Camera. *J. Geophys. Res.*, **123**, doi:10.1029/2018JD029390.
- 534 Trenberth, K. E., J. T. Fasullo, and J. Kiehl, 2009: Earth's global energy budget. *Bull. Am.*
535 *Meteor. Soc.*, **90**, 311–323, doi:10.1175/2008BAMS2634.1.



- 536 Wang, H. and W. Su, 2013: Evaluating and understanding top of the atmosphere cloud
537 radiative effects in Intergovernmental Panel on Climate Change (IPCC) fifth assessment
538 report (AR5) clouded model intercomparison project phase 5 (CMIP5) models using
539 satellite observations. *J. Geophys. Res.*, **118**, 1–17, doi:10.1029/2012JD018619.
- 540 Wielicki, B. A., B. R. Barkstrom, E. F. Harrison, R. B. Lee, G. L. Smith, and J. E. Cooper,
541 1996: Clouds and the Earth’s Radiant Energy System (CERES): An Earth Observing
542 System experiment. *Bull. Amer. Meteor. Soc.*, **77**, 853–868.
- 543 Wild, M., D. Folini, C. Schar, N. G. Loeb, E. G. Dutton, and G. Konig-Langlo, 2013:
544 The global energy balance from a surface perspective. *Clim. Dyn.*, **40**, 3107–3134, doi:
545 10.1007/s00382-012-1569-8.
- 546 Yang, Y., et al., 2018: Cloud Products from the Earth Polychromatic Imaging Camera
547 (EPIC): Algorithms and Initial Evaluation. *Atmos. Meas. Tech. Discussions*, 1–23, doi:
548 10.5194/amt-2018-316.
- 549 Zhang, J., S. A. Christopher, L. A. Remer, and Y. J. Kaufman, 2005: Shortwave aerosol
550 radiative forcing over cloud-free oceans from Terra: 2. Seasonal and global distributions.
551 *J. Geophys. Res.*, **110 (D10S24)**, D10S24, doi:10.1029/2004JD005009.



552 List of Tables

553	1	Summary of the cases included in the spectral radiance database. AOD is for	
554		aerosol optical depth, COD is for cloud optical depth.	25
555	2	Mean ratio and standard deviation (in parenthesis) of filtered radiance to	
556		unfiltered radiance for SW and NIR bands over different scene types.	26
557	3	SW flux comparisons between NISTAR and CERES SYN1deg for all coinci-	
558		dent observations of 2017. F_n is the NISTAR flux (in Wm^{-2}), F_s is the SYN	
559		flux (in Wm^{-2}), and $\frac{F_n - F_s}{F_s}$ is the relative difference between them (in %).	27
560	4	LW flux comparisons between NISTAR and CERES SYN1deg for all coinci-	
561		dent observations of 2017. F_n is the NISTAR flux (in Wm^{-2}), F_s is the SYN	
562		flux (in Wm^{-2}), and $\frac{F_n - F_s}{F_s}$ is the relative difference between them (in %).	28



TABLE 1. Summary of the cases included in the spectral radiance database. AOD is for aerosol optical depth, COD is for cloud optical depth.

Clear				
	AOD	Aerosol type	Surface	
Ocean	8	6	4	
Land	8	4	15	
Snow	5	2	5	
Cloudy				
	COD	Cloud type	Surface	Atmosphere
Ocean	7	4 liquid and 3 ice	4	4
Land	7	4 liquid and 3 ice	15	1



TABLE 2. Mean ratio and standard deviation (in parenthesis) of filtered radiance to unfiltered radiance for SW and NIR bands over different scene types.

	SW ratio (standard deviation \times 1000)					
	0.0	29.0	41.4	60.0	75.5	85.0
Clear Ocean	0.8659(1.0)	0.8660(1.0)	0.8661(1.1)	0.8664(1.2)	0.8669(1.0)	0.8674(0.8)
Clear Land	0.8694(0.6)	0.8693(0.6)	0.8692(0.6)	0.8690(0.5)	0.8687(0.5)	0.8685(0.8)
Clear Snow	0.8689(0.1)	0.8689(0.1)	0.8689(0.2)	0.8688(0.2)	0.8688(0.3)	0.8687(0.4)
Cld Ocean	0.8687(1.0)	0.8687(1.0)	0.8688(0.9)	0.8688(0.8)	0.8688(0.7)	0.8687(0.6)
Cld Land	0.8694(0.4)	0.8693(0.3)	0.8693(0.3)	0.8692(0.3)	0.8690(0.4)	0.8689(0.5)
	NIR ratio (standard deviation \times 1000)					
	0.0	29.0	41.4	60.0	75.5	85.0
Clear Ocean	0.8293(23.1)	0.8270(24.0)	0.8253(25.5)	0.8235(28.3)	0.8238(28.4)	0.8229(26.4)
Clear Land	0.8790(9.6)	0.8777(10.4)	0.8764(10.7)	0.8730(10.8)	0.8663(10.1)	0.8501(12.4)
Clear Snow	0.8360(1.7)	0.8360(1.8)	0.8361(1.9)	0.8363(2.1)	0.8370(2.8)	0.8365(6.0)
Cld Ocean	0.8557(3.2)	0.8555(2.6)	0.8562(2.4)	0.8567(3.1)	0.8565(4.4)	0.8539(7.9)
Cld Land	0.8627(8.2)	0.8624(7.8)	0.8621(7.3)	0.8613(6.2)	0.8598(4.8)	0.8566(6.2)



TABLE 3. SW flux comparisons between NISTAR and CERES SYN1deg for all coincident observations of 2017. F_n is the NISTAR flux (in Wm^{-2}), F_s is the SYN flux (in Wm^{-2}), and $\frac{F_n - F_s}{F_s}$ is the relative difference between them (in %).

	Jan	Feb	Mar	Apr	May	Jun	Jul	Aug	Sep	Oct	Nov	Dec
F_s	—	210.3	205.1	201.9	201.4	198.8	194.5	195.0	199.9	210.3	222.3	228.5
F_n	—	217.5	214.3	210.4	213.7	214.3	209.5	208.4	211.1	224.1	236.1	240.5
$\frac{F_n - F_s}{F_s}$	—	3.4	4.5	4.2	6.1	7.8	7.7	6.9	5.6	6.6	6.2	5.3



TABLE 4. LW flux comparisons between NISTAR and CERES SYN1deg for all coincident observations of 2017. F_n is the NISTAR flux (in Wm^{-2}), F_s is the SYN flux (in Wm^{-2}), and $\frac{F_n - F_s}{F_s}$ is the relative difference between them (in %).

	Jan	Feb	Mar	Apr	May	Jun	Jul	Aug	Sep	Oct	Nov	Dec
F_s	—	242.3	242.0	244.0	247.6	250.1	251.6	249.3	246.1	243.2	240.1	241.3
F_n	—	251.5	246.3	256.1	254.0	253.4	254.0	251.5	253.8	251.8	248.8	251.6
$\frac{F_n - F_s}{F_s}$	—	3.8	1.8	5.0	2.6	1.3	1.0	0.9	3.1	3.5	3.6	4.3



563 List of Figures

- 564 1 Schematic of a) Earth-Sun-DSCOVR geometry and b) Earth disc that are
565 visible to the L1 DSCOVR view (left with an area fraction of A_t) and to the
566 L2 view (right). The golden area on the left shows the daytime area fraction
567 (A_v) that are visible to DSCOVR, the black area on the left shows the night
568 portion (A_d) that are within the DSCOVR view, and the golden area on the
569 right is the daytime portion (A_h) missed by the DSCOVR. Not to scale. 31
- 570 2 NISTAR SW and NIR spectral transmission function. 32
- 571 3 EPIC RGB image for May 15, 2017 at 12:17 UTC (a), and the corresponding
572 total cloud fraction (b, in %). Liquid and ice cloud fractions are shown in
573 (c) and (d), liquid and ice cloud optical depths are shown in (e) and (f), and
574 liquid and ice cloud effective height (in km) are shown in (g) and (h). (b) to
575 (h) are all derived from the EPIC composite. 33
- 576 4 SW anisotropic factors (a) and LW anisotropic factors (b) derived from the
577 CERES ADMs using the EPIC composite for scene identification for May 15,
578 2017 at 12:17 UTC. 34
- 579 5 SW flux (blue) and LW flux (red) derived from NISTAR measurements for
580 April (a) and July (b), 2017. 35
- 581 6 An example of the daytime SW flux distributions from CERES SYN1deg
582 product at 10 UTC on January 1, 2017 (a), and the corresponding areas (in
583 red) that are visible to EPIC and the terminator boundary (in blue) (b). 36
- 584 7 SW flux (in Wm^{-2}) comparisons between NISTAR and CERES SYN for April
585 (a) and July (b) 2017. 37
- 586 8 LW flux (in Wm^{-2}) comparisons between NISTAR and CERES SYN for April
587 (a) and July (b) 2017. 38
- 588 9 Comparison of coincident hourly SW and LW fluxes from NISTAR and CERES
589 SYN1deg for 2017. Color bar indicates the number of occurrence. 39



590 10 Daily mean SW flux (a) and LW flux (b) comparisons between CERES SYN1deg
591 (blue) and NISTAR (red) for 2017. 40

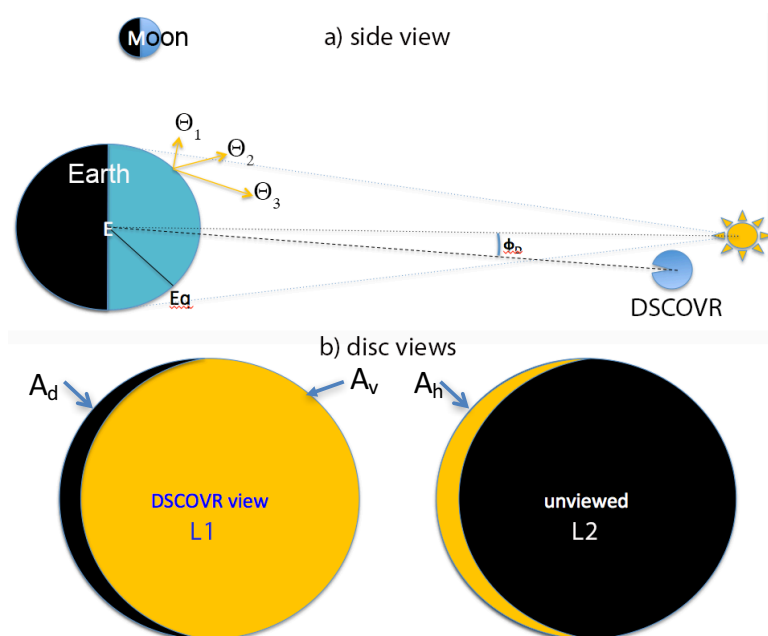


FIG. 1. Schematic of a) Earth-Sun-DSCOVR geometry and b) Earth disc that are visible to the L1 DSCOVR view (left with an area fraction of A_t) and to the L2 view (right). The golden area on the left shows the daytime area fraction (A_v) that are visible to DSCOVR, the black area on the left shows the night portion (A_d) that are within the DSCOVR view, and the golden area on the right is the daytime portion (A_h) missed by the DSCOVR. Not to scale.

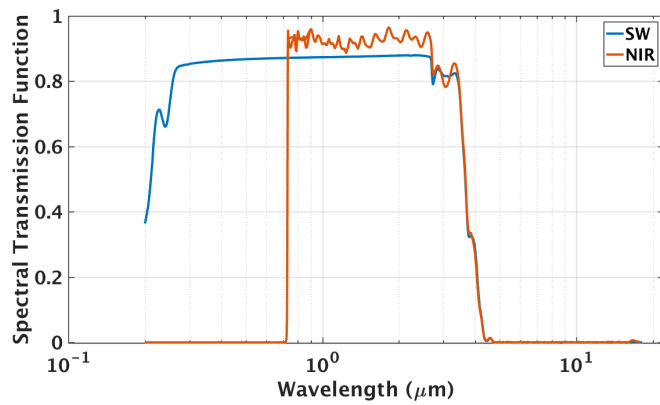


FIG. 2. NISTAR SW and NIR spectral transmission function.

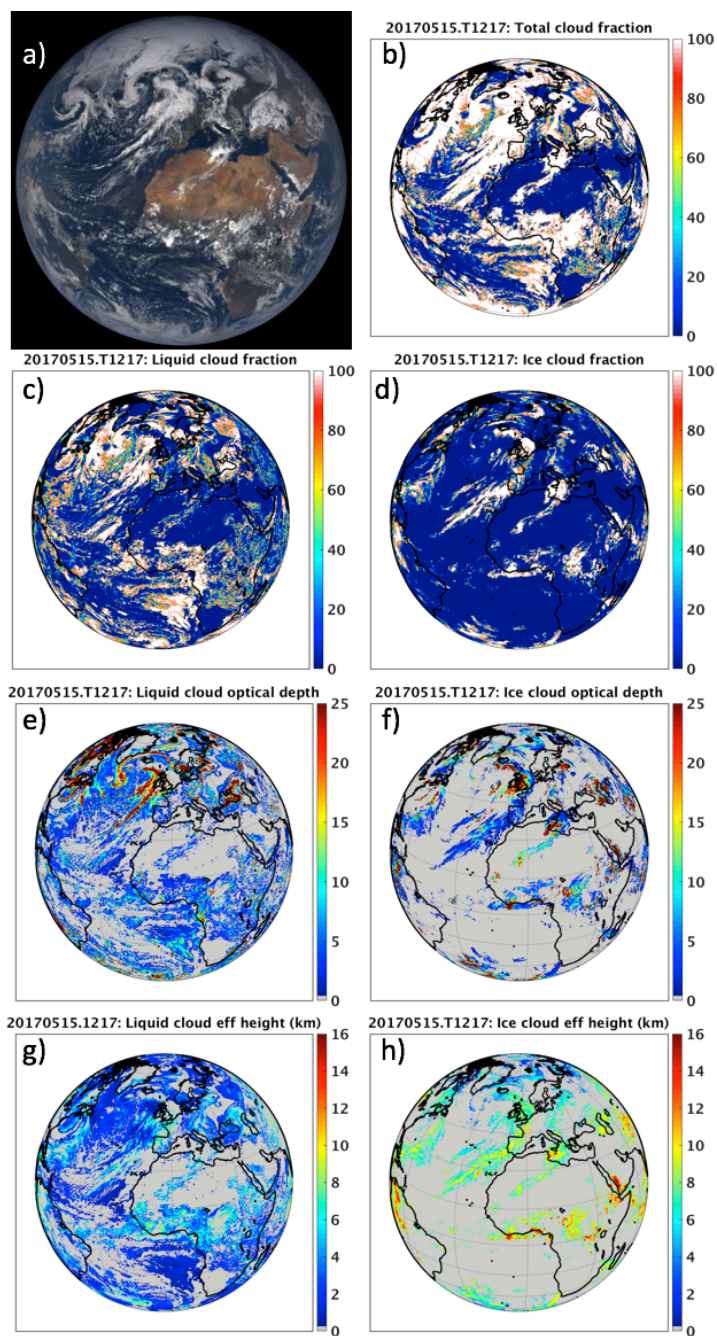


FIG. 3. EPIC RGB image for May 15, 2017 at 12:17 UTC (a), and the corresponding total cloud fraction (b, in %). Liquid and ice cloud fractions are shown in (c) and (d), liquid and ice cloud optical depths are shown in (e) and (f), and liquid and ice cloud effective height (in *km*) are shown in (g) and (h). (b) to (h) are all derived from the EPIC composite.

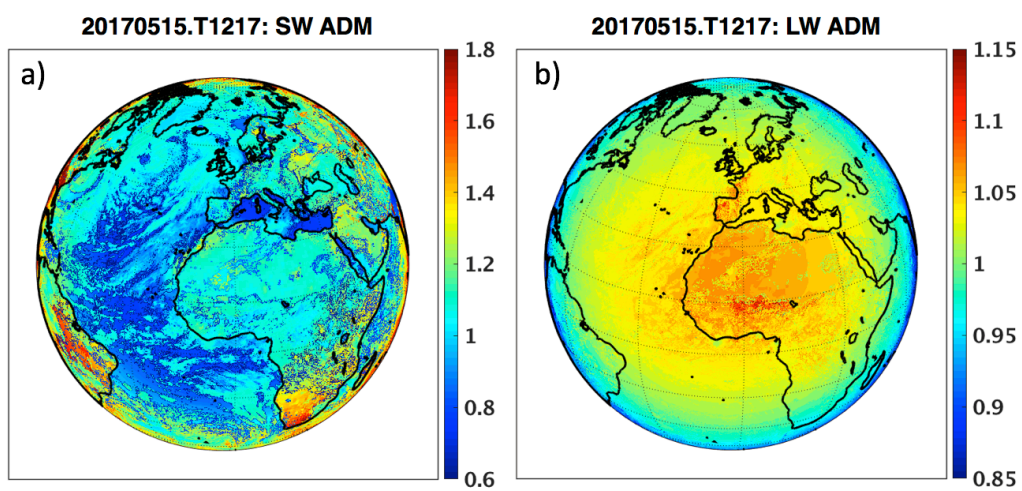


FIG. 4. SW anisotropic factors (a) and LW anisotropic factors (b) derived from the CERES ADMs using the EPIC composite for scene identification for May 15, 2017 at 12:17 UTC.

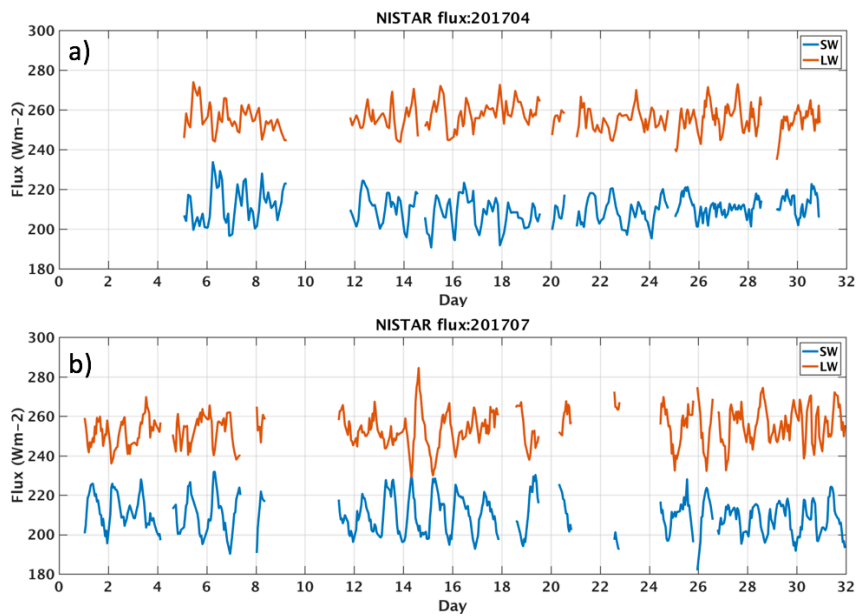


FIG. 5. SW flux (blue) and LW flux (red) derived from NISTAR measurements for April (a) and July (b), 2017.

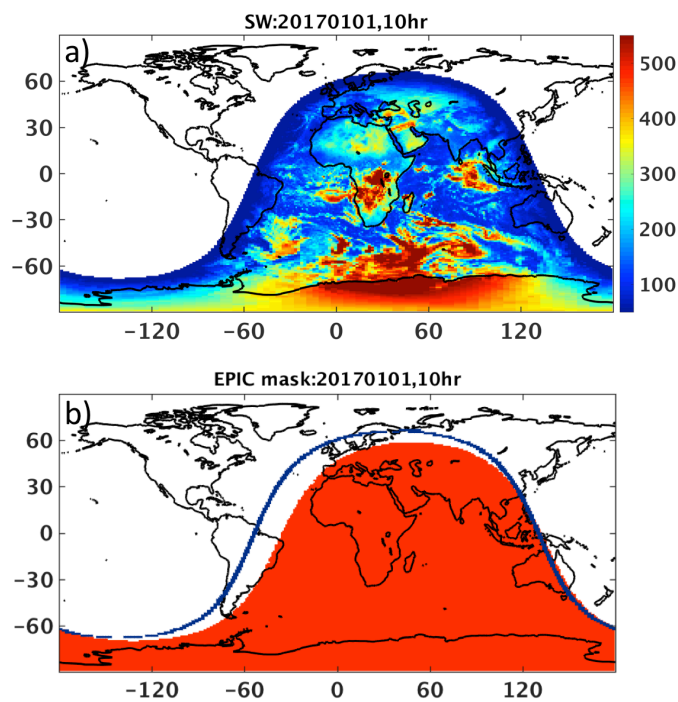


FIG. 6. An example of the daytime SW flux distributions from CERES SYN1deg product at 10 UTC on January 1, 2017 (a), and the corresponding areas (in red) that are visible to EPIC and the terminator boundary (in blue) (b).

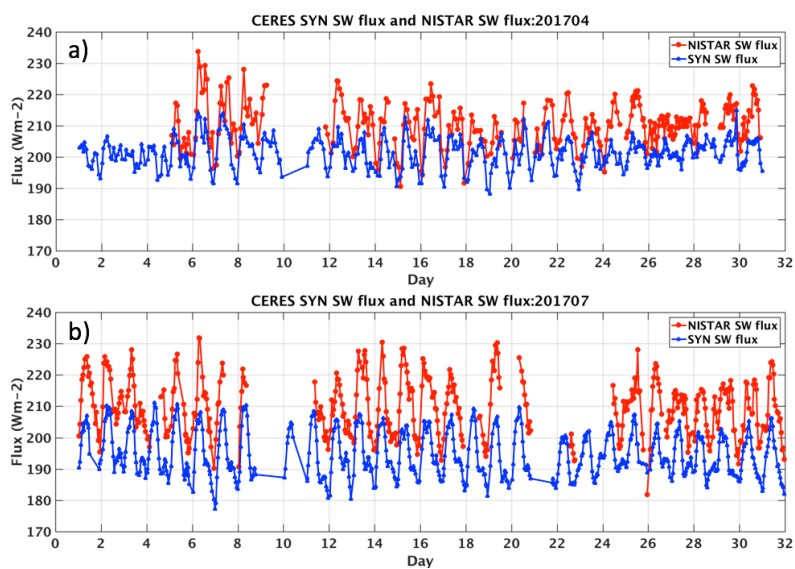


FIG. 7. SW flux (in Wm^{-2}) comparisons between NISTAR and CERES SYN for April (a) and July (b) 2017.

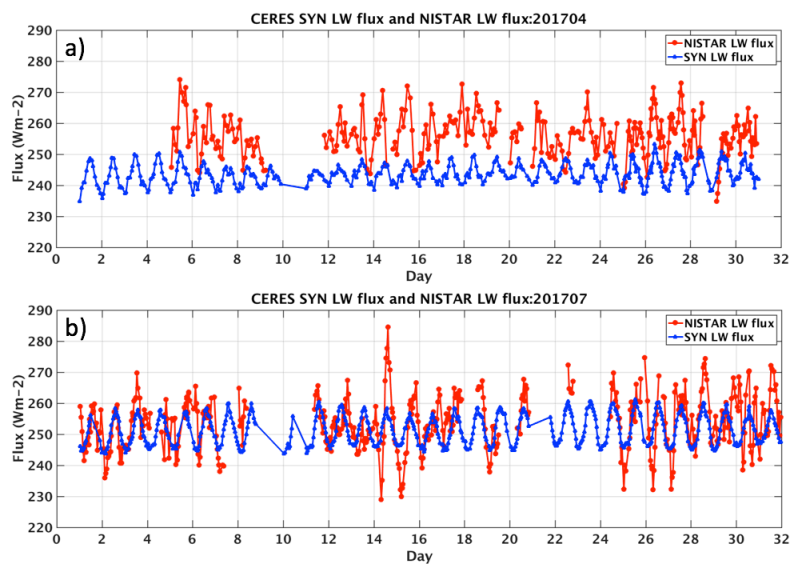


FIG. 8. LW flux (in Wm⁻²) comparisons between NISTAR and CERES SYN for April (a) and July (b) 2017.

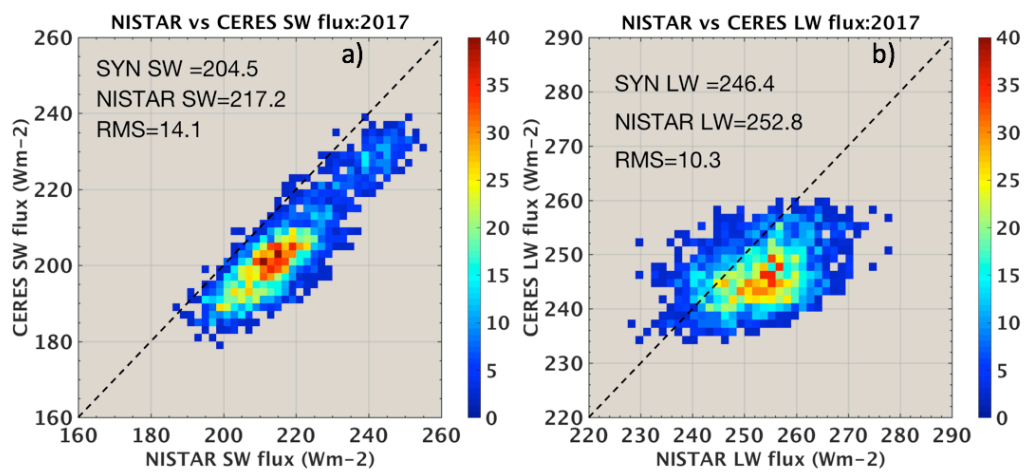


FIG. 9. Comparison of coincident hourly SW and LW fluxes from NISTAR and CERES SYN1deg for 2017. Color bar indicates the number of occurrence.

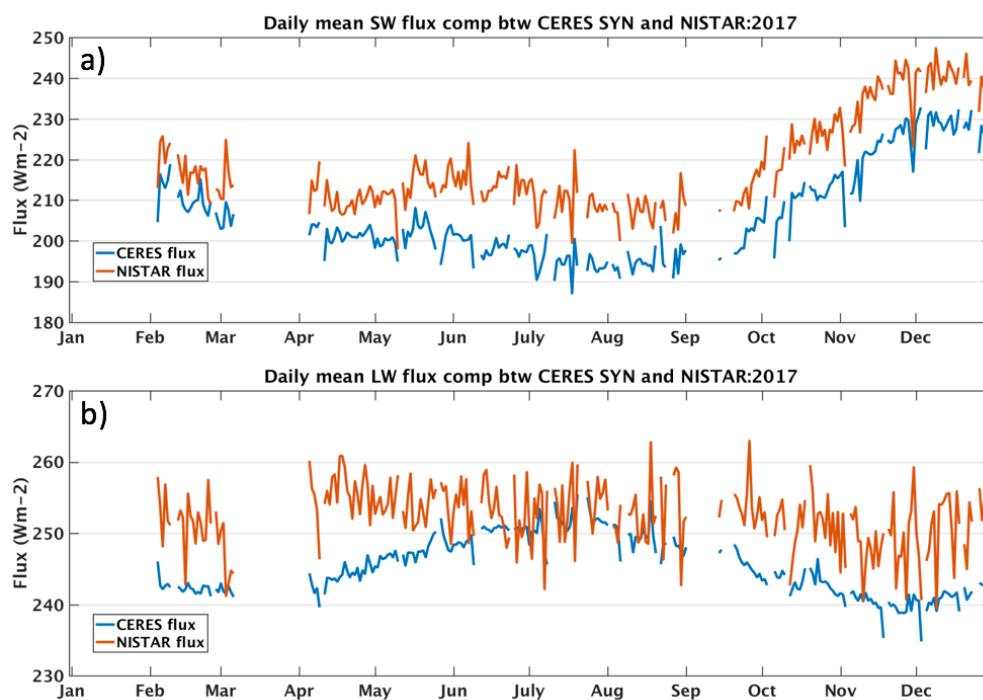


FIG. 10. Daily mean SW flux (a) and LW flux (b) comparisons between CERES SYN1deg (blue) and NISTAR (red) for 2017.